Carbon 115 (2017) 347–362

Contents lists available at ScienceDirect

Carbon

journal homepage: www.elsevier.com/locate/carbon

Protective effect of ultrathin alumina film against diffusion of iron into carbon fiber during growth of carbon nanotubes for hierarchical composites investigated by ptychographic X-ray computed tomography

W. Szmyt [a, b, c, d, *], S. Vogel [a, b, c], A. Diaz [b], M. Holler [b], J. Gobrecht [b], M. Calame [c, d], C. Dransfeld [a]

[a] Institute of Polymer Engineering, FHNW University of Applied Sciences and Arts Northwestern Switzerland, Klosterzelgstrasse 2, 5210 Windisch, Switzerland
[b] Paul Scherrer Institut, 5232 Villigen, PSI, Switzerland
[c] Department of Physics, University of Basel, Klingelbergstrasse 82, 4056 Basel, Switzerland
[d] Swiss Nanoscience Institute, University of Basel, Klingelbergstrasse 82, 4056 Basel, Switzerland

ARTICLE INFO

Article history:
Received 2 August 2016
Received in revised form
12 December 2016
Accepted 28 December 2016
Available online 4 January 2017

ABSTRACT

Composite materials based on carbon fiber (CF) are prone to failure at the fiber-matrix interface upon compression or stress transverse to the fiber axis. The direct growth of carbon nanotubes on CF constitutes a novel approach to enhance the mechanical properties of the interface. However, the challenge is that, during the growth, tensile properties of the fiber are altered due to the diffusion effect of iron nanoparticles used in the process, leading to CF surface defect formation. In this work, we deliver and discuss an analysis methodology on ptychographic X-ray computed tomography (PXCT) images in order to assess the iron nanoparticle abundance within CFs. PXCT provides 50 nm - resolved 3D electron density maps of the CFs. We evidence the protective effect of an ultrathin alumina film against iron infiltration into CF during the CNT growth. This method potentially allows to evaluate the efficiency of other diffusion-minimizing approaches. The conclusions of the PXCT examination are validated by energy-dispersive X-ray spectroscopy and scanning transmission electron microscopy carried out on thin sample slices cut with a focused ion beam. The results provide a new insight into the mechanical performance of CFs and therefore constitute valuable knowledge for the development of hierarchical composites.

1. Introduction

Carbon fiber reinforced polymers (CFRP) easily overcome the traditional metal solutions in terms of strength- and stiffness-to-mass ratio owing to their extraordinary tensile mechanical properties in the fiber direction. The failure of CFRP occurs typically at the fiber-matrix interface upon stress in the direction transverse to the CF or compression. Hierarchical composites constitute a novel approach to enhance the mechanical properties of the CF-based composites utilizing the direct growth of nanoscale carbon nanotubes (CNT) on the surface of the microscale CF with chemical vapor deposition (CVD) before the impregnation with the polymer [1]. The CNT CVD growth process is typically catalyzed by iron nanoparticles (NPs). The direct CNT growth on the CF is challenged by surface defect formation induced by the iron catalyst, leading to strongly altered tensile properties of the CF, because the tensile failure of the fiber often originates at a defect [2]. Qian et al. [3] have observed homogeneously distributed pits in the surface of a CF after CNT growth and subsequent chemical removal of iron. They related this effect directly to the defect-induced strength decrease. They have also come to a conclusion that dissolution of iron in CF along with the resulting defect formation occurs in the same CVD parameter window, as the efficient CNT growth, which has appeared as a challenge. In a later study, Qian et al. [4] have

* Corresponding author. Institute of Polymer Engineering, FHNW University of Applied Sciences and Arts Northwestern Switzerland, Klosterzelgstrasse 2, 5210 Windisch, Switzerland.
E-mail address: Wojciech.Szmyt@fhnw.ch (W. Szmyt).

http://dx.doi.org/10.1016/j.carbon.2016.12.085

experimentally verified that the strength of CF decreases significantly in the process, which supported the previous observations. Zhu et al. [5] have attributed the roughening of CF to recrystallization of CF surface and etching with hydrogen at CNT growth temperatures up to 750 °C, however they also state a hypothesis that at higher temperatures iron NPs diffuse into the CF body and thus get disabled as CNT growth catalyst. Sonoyama et al. [6] have tackled the challenge of iron dissolution in CFs and NP disactivation by introducing a novel two-step CVD process based on ferrocene, xylene and H_2S vapors, hypothesizing that the sulfur absorbed by iron minimizes the unwanted effects. However, the mechanical properties of such prepared hairy fibers have not been examined. Zhang et al. [7] have reported, that at the CVD processing temperature of 750 °C the tensile properties of the fibers do not change significantly, however this reasoning was based on results with unusually large error bars. The preservation of the tensile properties in the process is crucial for the hierarchical composites to supersede the classical CFRP, which has been recently addressed in ways such as the alternative choice of the catalyst system [8] [9], different CVD growth reaction mechanism [9], non-covalent fiber functionalization with polymeric coating [10] [11], or application of a protective alumina film prior to coating with the catalyst [11], [12]. The latter was the subject of our recent study where we have shown that the application of an 11 nm thick alumina layer as a first processing step preserves the mechanical strength of the fiber during CNT growth [12]. For the convenience of the reader, the results are described briefly in Appendix B, see Fig. B 1. Degradation of high tensile strength carbon fiber coated with 0.1–5 μm thick nickel films upon CVD processing conditions has been studied by Warren et al. [13], where the diffusion-controlled carbon dissolution in metal and precipitation have been pointed out as the main mechanisms governing the process. The diffusion of iron particles into CFs at CVD processing temperatures is not well understood yet. In a previous work we presented 3D electron density maps of CF sections with and without alumina protective layer with a resolution of about 50 nm [14]. Measurements were done using ptychographic X-ray computed tomography (PXCT) [15] [16], with a high-resolution instrument [17]. Here, we introduce a methodology of quantitative assessment of iron NP abundance below the surface of the CF that overcomes the challenge that the NPs are not resolved in the PXCT measurements. The results of this novel method of 3D imaging and the unprecedented data analysis approach are confirmed by means of energy-dispersive X-ray spectroscopy (EDX), scanning electron microscopy (SEM) and scanning transmission electron microscopy (STEM) carried out on thin transverse slices of CFs cut with a focused ion beam (FIB). The results prove the protective effect of the thin alumina film against iron diffusion into CFs.

2. Experimental

The CFs that were used in the experiments were the commercially unsized and oxidative treated type of AS4 produced by Hexcel, USA, as used by Steiner et al. [11]. The CFs have been coated with alumina of two different thicknesses using the atomic layer deposition (ALD) technique [12], [18]. The iron catalyst has been deposited with a metal sputtering method on such prepared CFs as well as on a neat CF. Afterwards, the CNT growth has been carried out using a CVD technique based on hydrocarbon thermal decomposition. The sample preparation was equivalent to the one discussed in our previous work [14] and its detailed description is included in Appendix A for the convenience of the reader. The set of the prepared samples is summarized in Table 1. EDX elemental characterization and STEM imaging have been performed as a validation of the PXCT results. CF slices of ~100 nm thickness were cut using FIB in order to enable a clear identification of the positions of iron NPs by STEM for the subsequent analysis. A pristine CF was taken as a control sample. Subsequently, the PXCT imaging of the samples has been performed in order to assess the abundance of iron NPs within the fibers and thus evaluate the protective effect of the alumina film. Afterwards, EDX elemental characterization and STEM imaging has been performed as a validation of the PXCT results. CF slices of ~100 nm thickness were cut using FIB in order to enable a clear identification of the positions of iron NPs by STEM for the subsequent analysis.

Table 1
Summary of carbon fiber samples.

Sample name	Alumina ALD	Iron sputtering	CNT growth
Pristine	None	None	None
Unprotected	None	5 nm	Done
11 nm protected	11 nm	5 nm	Done
500 nm protected	500 nm	5 nm	Done

2.1. Single fiber imaging using ptychographic X-ray computed tomography

X-ray ptychography is a coherent diffraction imaging technique in which the specimen is scanned across a coherent finite illumination in such a way that adjacent illumination areas partially overlap [19]. At each scanning position, coherent diffraction patterns are recorded in the far field and used in phase retrieval algorithms to reconstruct the complex-valued transmissivity of the specimen, providing an image with both absorption and phase contrast [20]. Many such phase images acquired at different incidence angles of the specimen with respect to the incoming beam can be then combined tomographically to yield the 3D electron density distribution within the sample [15].

PXCT measurements were carried out at the cSAXS beamline of the Swiss Light Source at the Paul Scherrer Institut in Villigen, Switzerland, with a photon energy of 7 keV. We used a recently developed instrument that makes use of laser interferometry for high-accuracy positioning of the specimen with respect to the illuminating optics [17]. Details about the experimental setup and data acquisition can be found in Ref. [14], but for the reader's convenience we write the experimental parameters in Appendix C. All samples were measured as described in Ref. [14], except that for the pristine CF 250 projections were recorded instead of 375, as the absence of CNTs around the pristine CF yielded a lateral size significantly smaller compared to the other samples. We estimate that a dose of 3.4×10^7 Gy was imparted on the pristine specimen and 5.1×10^7 Gy on all other specimens. This difference in dose has basically no effect in the measurements in terms of resolution or radiation damage, as we do not expect radiation damage for these specimens. Ptychographic reconstructions were performed using a difference map algorithm [21] followed by a maximum likelihood optimization as a refinement step [22]. For the reconstructions we first used an area of 800 × 800 pixels of the recorded diffraction patterns for the pristine CF, obtaining a pixel size of 9.47 nm in the reconstructed images. As it became apparent that the resolution of the images was significantly worse, about 50 nm, for the other samples we used 600 × 600 pixels of the diffraction patterns, obtaining a pixel size of 12.62 nm. The phase images were further corrected for zero and first order terms and registered in the vertical direction as described in Ref. [23], and registered in the horizontal direction by tomographic consistency [24] to obtain 3D electron density maps. The 3D resolution was estimated to be about 50 nm comparing the Fourier shell correlation of two subtomograms with half the number of projections with the half-bit threshold [25].

2.2. Examination of thin carbon fiber slices with FIB/STEM/EDX for the purpose of validation of PXCT data analysis results

PXCT examination gives a vast amount of spatial information about the sample, being a non-destructive imaging method. Additionally, the unprecedented 3D image analysis approach introduced and discussed in the further part of the work allows overcoming the challenge that the sizes of iron NPs are below the resolution of the imaging method. Considering the magnitude of novelty in using PXCT for this purpose, it was decided to validate the results by another method that is well-established. Moreover, due to the fact that PXCT gives no information about the elemental composition, this aspect needed to be verified as well. The method of our choice for validation is FIB/STEM/EDX examination of thin fiber slices, which has been carried out in a Helios NanoLab™ 650 DualBeam™ microscope produced by FEI Company. The details of the FIB cutting procedure can be found in Appendix D. Two samples were examined: the unprotected one and the one protected with 11 nm alumina.

3. Results and discussion

3.1. Examination of CNT growth effect by means of scanning electron microscopy

Scanning electron microscopy (SEM) has been carried out in order to examine the result of CNT growth and to observe the iron NPs on the CF surface using Zeiss Supra VP55 high resolution field emission scanning electron microscope. It has been estimated from the SEM image that the iron NP diameters fall between 20 and 40 nm, whereas the areal density of the NPs is approximately equal to 6×10^{10} cm^{-2}, see Fig. 1. Moreover, the CNT morphology exhibits bamboo-shaped structures.

3.2. Assessment of the electron density of the materials present in the samples for the purpose of PXCT data analysis

The theoretical electron density of a material can be calculated using equation

$$\varrho = \frac{\Delta N_e}{\Delta V} = \frac{N_A d}{\mu} \sum_i N_i Z_i \qquad (1)$$

where ϱ is the electron density, d is the mass density of the material, N_A is the Avogadro number, μ is the molar mass of a stoichiometric unit of the material, i is the index of an element present in the material, N_i is the number of atoms of the i-th element in a stoichiometric unit of the material and Z_i is the atomic number of the element. The materials to consider in our case are the bulk of carbon fiber, iron in NPs assumed to be in a ferrite phase at room temperature, and alumina in the barrier layer. The CNTs and iron within CNTs are not considered because these nanostructures are not resolved in enough detail in the PXCT electron density maps. Besides, iron within CNTs or CNT morphology do not influence fiber strength, contrarily to iron NPs within the CF body, therefore their analysis is beyond the scope of this work. Table 2 is partially reproduced from our previous work [14] and summarizes the parameters of the considered materials. Cementite (Fe_3C) is added to the table of materials as it has been reported in literature that it can at least partially participate as intermediate species in the process of iron-catalyzed graphitization of amorphous carbon [26], [27].

For the sake of simplicity, in this work we assume that the NPs are composed of pure iron. This assumption does not alter the results significantly, as the difference between the electron densities of ferrite and cementite is smaller than 2%. Fig. 2 presents representative tomographic cross sections of the four samples obtained by PXCT. The values in Table 2 show that the electron density of iron is more than four times greater than that of CF. Therefore it is reasonable to attribute the voxel groups of elevated electron density in Fig. 2b to iron NPs within the unprotected CF. This effect is not visible in the other three electron density maps. The 11 nm alumina film is not clearly visible in Fig. 2c, because the thickness of the film is smaller than the PXCT resolution and the electron density of the alumina is not more than twice the one of the CF. Instead, only a slightly elevated electron density on the CF surface is observed. It is non-trivial to determine how much it is influenced by the presence of the alumina or by the iron NPs condensed on the surface. Nonetheless, the high-density voxels are always on the surface of a CF and never underneath it, which is in agreement with the hypothesis of the diffusion-blocking effect of the 11 nm alumina film. A detailed analysis of iron NP abundance is carried out in the further part of this work. The 500 nm alumina film is easily resolved in the images and such prepared samples exhibit no presence of iron below the CF surface, as shown in Fig. 2d. The electron density of the alumina has been measured to be 0.82 Å^{-3} which is in a good agreement with the corresponding value 0.89 Å^{-3} form Table 2.

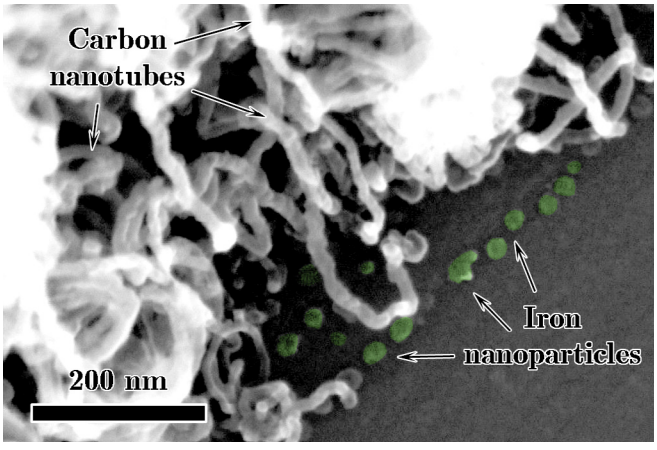

Fig. 1. SEM image of iron NPs (coloured in green for visibility) and CNTs grown on the surface of a CF. (A colour version of this figure can be viewed online.)

3.3. Fitting of cylindrical mask to CF for spatial data analysis of 3D PXCT images

The 3D electron density maps of each sample consist of stacks of equally-spaced 2D slices approximately perpendicular to the fiber axis, which is almost parallel to the rotation axis, z. For the sake of generality and greater accuracy, the CFs are assumed to have an elliptical cross section. To analyze the data we fit an elliptic cylinder to the CF section with an automated algorithm. This is performed the following way:

- The largest ellipse which fits inside the CF is sought for each slice. The ellipse is defined by

$$\mathbf{r}(\vartheta) = \mathbf{r}_0 + \begin{pmatrix} \cos\vartheta_0 & \sin\vartheta_0 \\ -\sin\vartheta_0 & \cos\vartheta_0 \end{pmatrix} \begin{pmatrix} a\sin\vartheta \\ b\cos\vartheta \end{pmatrix}, \quad \vartheta \in [0, 2\pi). \qquad (2)$$

Table 2
Properties of the materials considered within this work. The body of the CF is predominantly composed of C and N, its stoichiometry is taken as fractional. Densities are given at room temperature.

Material	Density[a]/g cm^{-3}	Stoichiometry	Molar mass/g mol^{-1}	Atomic numbers	Electron density[b]/Å^{-3}
alumina	3.00[c]	Al_2O_3	101.96	$_{13}$Al, $_{8}$O	0.89
CF	1.79[d]	$C_{0.95}N_{0.05}$[d]	12.11	$_{6}$C, $_{7}$N	0.54
ferrite	7.88[e]	Fe	55.85	$_{26}$Fe	2.21
cementite	7.70[f]	Fe_3C	179.55	$_{26}$Fe, $_{6}$C	2.17

[a] Given at room temperature.
[b] Calculated using equation (1).
[c] Density of alumina ALD film obtained at 177 °C by Groner et al. [28].
[d] Atomic fractions of the respective elements in the CF composition, calculated using the data from Hexcel©, HexTow® AS4 Carbon Fiber Product Data Sheet 2016 available at http://www.hexcel.com/Resources/DataSheets/Carbon-Fiber-Data-Sheets/AS4.pdf.
[e] Calculated using crystallographic data obtained by von Batchelder et al. [29].
[f] Calculated using crystallographic data obtained by Wood et al. [30].

where ϑ is the angular argument, $\mathbf{r}$ is the position vector of the ellipse point for the given ϑ, $\mathbf{r}_0$ is the position vector of the geometric center of the ellipse, ϑ_0 is the angle of rotation of the ellipse, a and b are the ellipse axes, as shown in Fig. 3. The size parameter of the ellipse is defined as $a^2 + b^2$. The ellipse is considered to be inside the CF if all the voxels intersected by the ellipse have an electron density not lower than the threshold 0.4 Å^{-3}. This value was chosen arbitrarily as smaller than the CF electron density giving the best fitting results and it can be adjusted to the needs of a specific case. As a result, the algorithm returns a set of parameters for each slice: a, b, ϑ_0, $\mathbf{r}_0$.

- The lengths of the axes and the ellipse rotation angle are calculated as mean values of a, b, and ϑ_0 from all 2D slices. The center position is calibrated using a linear fit of $\mathbf{r}_0$ as a function of the z coordinate of each slice.
- The distance from the ellipse edge is assigned to each voxel for the purposes of further spatial image analysis, which constitutes a so-called distance map.

If the CF axis was significantly deviated from the perpendicular to the map axis z, it would be necessary to account for this deviation in the analysis. However, in practice this angle never deviated from the parallel by more than 1°, therefore it was convenient to assume that the fiber axis is perpendicular to the slices. Such an approximation introduced a maximum relative systematic error in the x, y coordinates within each slice of $1/\cos(1^\circ)-1 \approx 2 \times 10^{-4}$. The corresponding spatial error is estimated by multiplication of the nominal radius of the CF of 3.5 μm by the relative error, giving 0.7 nm. This value is much smaller than the spatial resolution of about 50 nm, therefore we claim that the approximation does not yield a significant error of voxel positions within each slice. However, because the distance between the extreme tomography slices is as large as 8.2 μm, the subtle tilt of the fiber axis leads to a maximum shift between the CF cross sections of 8.2 μm·tan 1° ≈ 140 nm, which is already significant. Therefore, for the purposes of the analysis, the only necessary transformation was the calibration of the center of the elliptical CF cross sections. Effectively, the distances of each voxel from the ellipse edges can be considered as the distances from the cylinder wall and a 3D distance map is obtained.

3.4. Histograms of electron density

To investigate the presence of iron within the carbon fiber with and without the alumina protection film, it is necessary to analyze the electron density distributions. The histograms of voxels from 650 tomographic slices corresponding to 8.2 μm long fragments of CFs with and without the thin alumina film have been prepared as a function of electron density and distance from the CF edge, namely

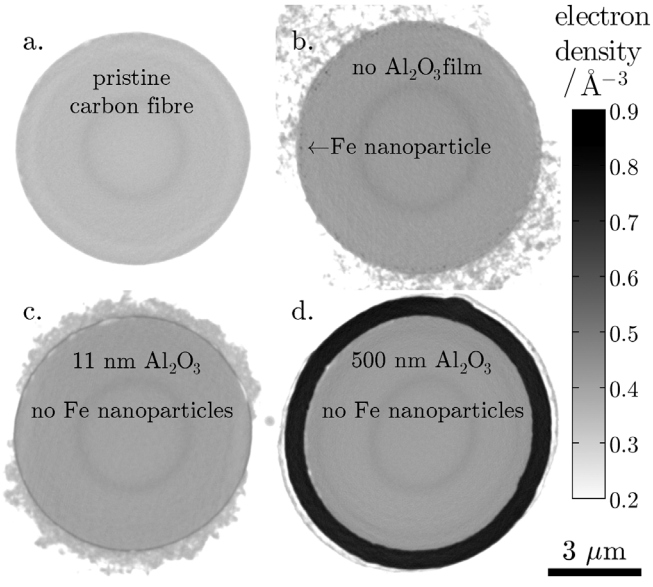

Fig. 2. Representative averages over 25 subsequent slices of electron density maps of CFs with a total thickness of about 328 nm; (a) pristine carbon fiber control sample; (b) unprotected CF grafted with CNTs exhibiting presence of iron NPs below its surface; (c) CF with 11 nm alumina film showing no iron NPs below the surface; (d) CF with 500 nm thick alumina film showing no presence of iron below the fiber surface.

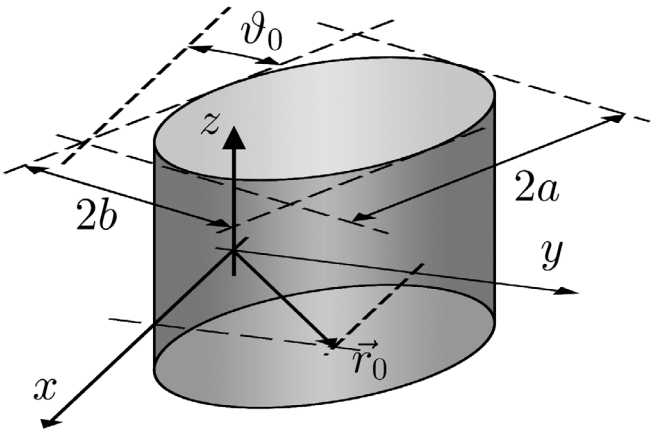

Fig. 3. Illustration of the geometric parameters of the fiber orientation and dimensions discussed in section 3.3. The cylinder represents the fiber surface. The xy plane is the plane of tomography slices, whereas the z axis is the axis of rotation. The fiber axis is deviated from z by not more than 1°.

depth into the CF, and are shown in Fig. 4.

Although iron has a nominal electron density of 2.21 $Å^{-3}$, in the histograms we cannot explicitly resolve any high electron density peak that would correspond to such a high value. This is due to the fact that the size of the NPs is below the resolution of the 3D image. Physically, iron NP constitutes a highly localized spot of elevated electron density with respect to the surrounding body of a CF. Due to the resolution limitation, the image of the original physical object is smoothened with a so-called point spread function (PSF). Effectively, if the PSF width is comparable to- or greater than the NP diameter, the high electron density values are not even present in the images. Instead, in the histogram of the unprotected carbon fiber one can notice an effect of a long shoulder reaching elevated electron densities up to about 0.9 $Å^{-3}$ at depths around 0.1 μm. Such an effect was not observed for the protected CF or at depths greater than 0.3 μm for the unprotected CF, therefore we reason that it represents the abundance of iron NPs. In the following we introduce a methodology that allows investigating the size distribution of NPs as a function of the depth into the CF, despite the fact that they are unresolved in the measurement.

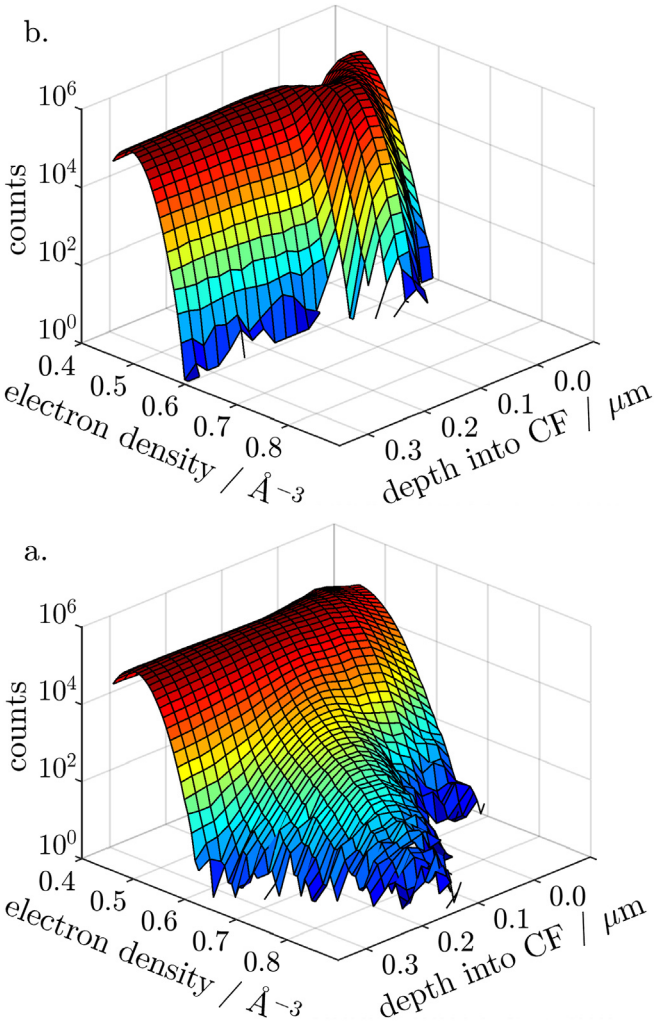

Fig. 4. Sample without (a) and with (b) an 11 nm thick protective alumina film - surface plots of histograms of voxels versus depth into CF and electron density. A high electron density shoulder is visible only for the unprotected CF, which is related to presence of iron below its surface. (A colour version of this figure can be viewed online.)

3.5. Assessment of the resolution blur from PXCT data

Although the voxel size is 12.62 nm, the effective resolution of the 3D images acquired by PXCT is about 50 nm, limited by the density contrast of the features within the sample and by the dose, which limits the maximum angle of the X-rays scattered and measured with sufficient signal-to-noise ratio. Besides the voxel size and electron density noise, we include the effect of a PSF which accounts for this resolution limit. All three mentioned factors result in the resolution of 50 nm estimated using the Fourier shell correlation of two subtomograms with a half-bit threshold as described in Ref. [25]. Even though the measurement resolution is defined, an explicit form of the point spread function that blurs the image in our measurements remains unknown and its estimate is crucial for the further analysis of the abundance of the unresolved iron NPs.

In order to investigate the behavior of the point spread function in the plane perpendicular to the rotation axis, we examined the electron density profile at a well-defined interface between the carbon fiber and the 500 nm alumina film. We have evaluated a mean cross section along 650 slices and extracted an electron density profile as a function of the depth into the CF. Assuming that the interface is locally flat and sharp, one can extract the profile of one-dimensional PSF

$$p(x) = \int_{-\infty}^{\infty} h(x-\tau)\mathrm{PSF}(\tau)\mathrm{d}\tau = \int_{-\infty}^{x} \mathrm{PSF}(\tau)\mathrm{d}\tau \Rightarrow \mathrm{PSF}(x) = \frac{d}{dx}p(x), \tag{3}$$

where $p(x)$ is the measured edge profile and $h(x)$ is the Heaviside step function. It needs to be pointed out that because the PSF is a three-dimensional function, such a way of extracting the PSF does not produce an explicit curve, but is rather useful to qualitatively examine the general behavior of the function in the radial direction. The results are shown in Fig. 5.

The profile in Fig. 5 has been obtained as mean values of electron density of all the voxels of the 3D map that fall spatially within the range of depths into the CF between x_i-Δ/4 and x_i+Δ/4, where i indexes the points of the graph and Δ is the PXCT cubic voxel size equal 12.61 nm. The derivative has been calculated using a five-point numerical differentiation. The result shows that, although there are ripples visible in the PSF, it might be well described with a Gaussian of standard deviation equal to 31.04 ± 0.34 nm. The ripples may be neglected since in the case of the barely resolved iron NPs, they generate deviations in electron density well below the noise level.

Because of the rotational character of the measurement and tomographic reconstruction procedure, an anisotropy of resolution between the radial and the axial direction might appear. In order to estimate the axial blur and crosscheck the value of the radial blur, we introduce an approach that relies on analysis of features significantly larger than the experimental resolution. In the tomograms of the hairy fibers one can notice several ball-shaped structures of diameter ~500 nm of a uniform electron density slightly lower than the one of the CF, see Fig. 6. We have used such features to assess the blur in three dimensions assuming that the PSF is estimated by a 3D radial-symmetric Gaussian kernel defined as

$$G(r,z) = \frac{1}{(2\pi)^{3/2}\sigma_r^2\sigma_z}\exp\left(-\frac{r^2}{2\sigma_r^2} - \frac{z^2}{2\sigma_z^2}\right), \tag{4}$$

where σ_r and σ_z are the standard deviations of the Gaussian kernel

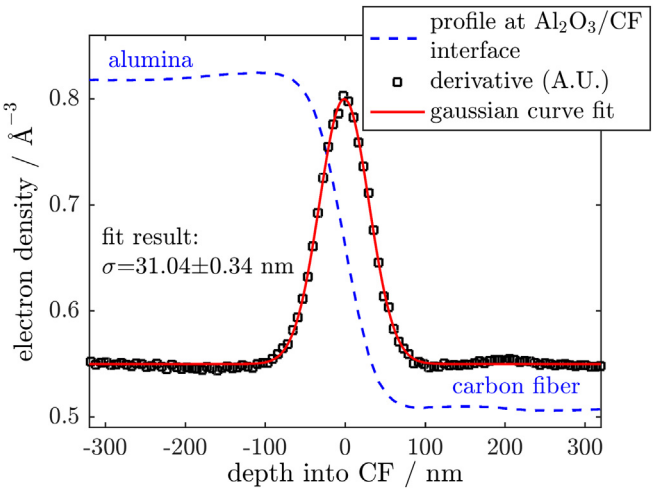

Fig. 5. Electron density profile of the interface between CF and alumina on the sample coated with 500 nm alumina (blue dashed line) and its derivative representing the rough estimate of the point spread function in lateral direction (black squares) along with the Gaussian curve fit (red solid line). The derivative is scaled in arbitrary units and translated to fit in the graph. (A colour version of this figure can be viewed online.)

in radial and axial directions, respectively. Effectively, an anisotropy in PSF between the radial and the axial direction of the blur is assumed.

The method relies on finding a closest reproduction of the experimental map of a given feature using an optimization algorithm finding a minimum of the mean square deviation of a reproduced map from the experimental map. The mean square deviation is calculated in the following way:

1. Thresholding of the experimental map using an electron density threshold ϱ_T resulting in a 3D binary matrix.
2. Multiplication of the binary matrix by a defined electron density ϱ.
3. Convolution of the matrix with a 3D Gaussian with given σ_r and σ_z, resulting in a simulated map.
4. Calculation of the mean square deviation of the simulated map from the experimental map.

Effectively, the mean square deviation is a function of ϱ_T, ϱ, σ_r and σ_z and a minimum of this function is found using the fminsearch() function implemented in MATLAB and Optimization Toolbox Release 2016b, The MathWorks, Inc., Natick, Massachusetts, United States, relying on the simplex search method with 10^{-4} tolerance of the function value and arguments [31]. Effectively, ϱ_T, ϱ, σ_r and σ_z constitute a set of the fit parameters. Their initial values were set to 0.2 Å^{-3}, 0.4 Å^{-3}, 30 nm, 25 nm, respectively. The procedure was repeated for 11 extracted features resulting in a set of 11 corresponding σ_r and σ_z values. Effectively, $\sigma_r = 31.7 \pm 3.5$ nm and $\sigma_z = 26.9 \pm 3.2$ nm have been obtained, which represent mean values ± double standard deviation of the obtained value set. One slice of a representative feature image and its simulation using the parameters fitted to this particular feature is shown in Fig. 7.

There is a good agreement between the estimate of radial component of the blur obtained with this method and with the sharp interface profile analysis, which constitutes an ensuring cross-check of the blur value. A two-sample Kolmogorov-Smirnov test was carried out in order to verify the hypothesis that σ_r and σ_z come from the same distribution. The hypothesis was rejected at a 5% significance level (p-value equal 6.6×10^{-6}), therefore we can say that the axial-radial anisotropy of the blur is significant and an anisotropic Gaussian blur needs to be applied for the following analysis.

3.6. Methodology of assessment of abundance of iron nanoparticles from PXCT 3D images

In order to assess the amount of iron infused into the CF we have developed a self-consistent algorithm that reproduces the experimental electron density distributions in a simulation. We assume that the resolution exhibits a Gaussian behavior, which means that sharp physical features in the images are Gaussian-blurred with the radial σ_r and axial σ_z values estimated in section 3.5. The measurement noise is assumed to be Gaussian as well and it is added to the electron density of the voxels after the blur.

Initially, a set of maps of NPs of volumes v ranging from 0 to 15×10^4 nm^3 with a $\Delta v = 5 \times 10^3$ nm^3 increment is prepared. The NPs are assumed to be spherical and are defined by a step function with values ranging from 0, meaning lack of iron in a given voxel, to 1 meaning 100% of iron in the voxel. Each NP is defined on a

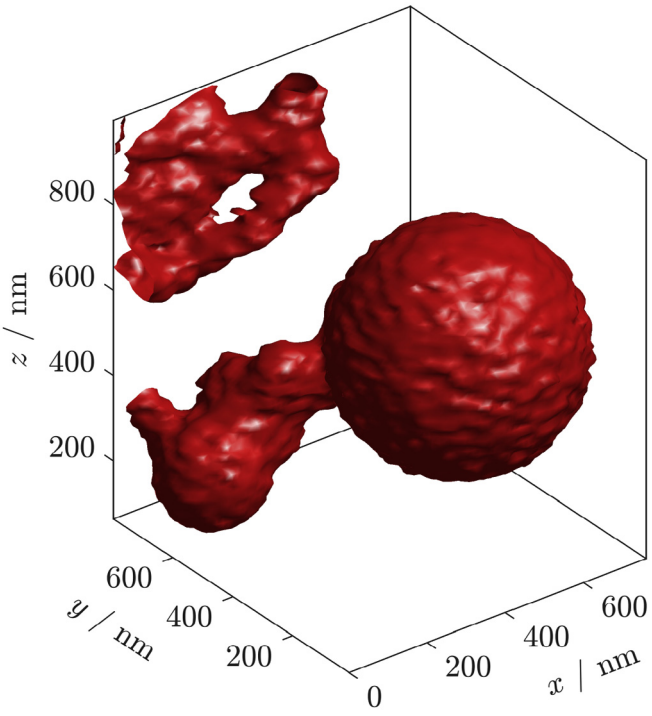

Fig. 6. One of the spherical-shaped features found in an unprotected carbon fiber tomogram used for resolution assessment. An isosurface render is shown at an electron density of 0.2 Å^{-3}. (A colour version of this figure can be viewed online.)

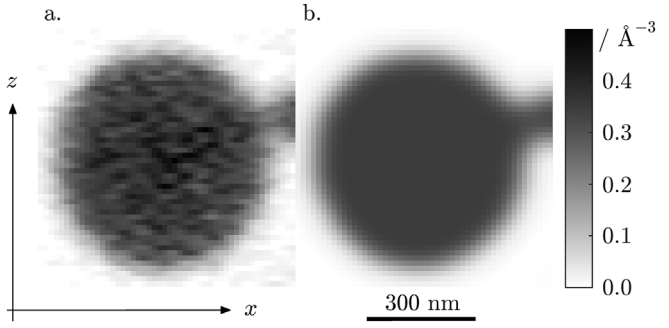

Fig. 7. A representative slice of an example reproduction result; (a) the experimental map, (b) the map simulated using the resulting parameters after the fit to this particular feature: $\sigma_r = 30.9$ nm, $\sigma_z = 27.3$ nm, $\varrho_T = 0.19$ Å^{-3}, $\varrho = 0.41$ Å^{-3}.

Cartesian 3D grid with $\delta = 3.155$ nm voxel size being 4 times smaller than the experimental voxel size Δ. Each electron density map is a cube of volume $V = 252.4^3$ nm^3 corresponding to the side equal $8 \times \sigma_r$ of the radial component of the blur. The cubic map with a NP of $v = 0$ corresponds to a cube of pure carbon fiber material. The electron density maps are numerically convolved with a three dimensional Gaussian kernel of radial $\sigma_r = 31.7$ nm and axial $\sigma_z = 26.9$ nm.

Having generated the set of maps of NPs of different sizes blurred with a given Gaussian function, we have defined a self-consistent algorithm that finds a distribution of iron NP volumes in the given volume of the experimental electron density map by reproducing the experimental electron density histogram in the simulation. The algorithm utilizes a random walk of the simulation parameters, namely the electron density of the CF ϱ_{CF}, the rms of the electron density noise and $f(x, v)$, which is the function that constitutes a distribution of NPs with respect to their volume v and depth into the CF x that need to be taken in order to produce the simulated electron density histogram resembling the experimental one presented in Fig. 4a. The function is defined as

$$dn(x, v) = f(x, v)dxdv, \tag{5}$$

where $dn(x, v)$ is equal to the areal density of NPs of volumes $(v, v + dv)$ within a slice of volume in a range of depths $(x, x + dx)$. The distribution is related to the number of voxels being drawn randomly from a NP map

$$N_{drawn}(x_i, v_j) = [VN_H(x_i) \cdot f(x_i, v_j)\Delta v], \tag{6}$$

where the square bracket represents rounding, $N_H(x_i)$ is the number of voxels of the experimental map taken to produce the histogram for a given x_i. The random draw is done in such a way that all the draws are independent. In other words the voxels drawn are allowed to repeat. The distribution f is kept normalized at all times so that the total number of voxels being randomly drawn is equal to $N_H(x_i)$ at each depth x_i individually. When f is found, it can be used to determine the atomic concentration of iron with respect to the depth into the CF,

$$c(x) = \frac{d_{Fe}N_A}{\mu_{Fe}} \int_0^{v_{max}} vf(x, v)dv, \tag{7}$$

where d_{Fe} is the mass density of iron, N_A is the Avogadro number, μ_{Fe} is the molar mass of iron, v_{max} is the maximum of the discrete mesh of NP volumes. Furthermore, to check how much of iron has infused into the CF during the process compared to the sputtered 5 nm iron film, one can calculate an equivalent film thickness

$$t \approx \int_0^{x_{max}} \int_0^{v_{max}} vf(x, v)dxdv \tag{8}$$

where t is the equivalent film thickness, x_{max} is the maximum depth into the CF taken into consideration. The approximation in equation (8) holds when $x \ll \inf\{a^2/b, b^2/a\}$ because it has been derived assuming that the radius of curvature of the CF surface is much larger than x.

The initial values of the simulation parameters are arbitrary and they reflect the further convergence efficiency. The initial values of the parameters resulting in relatively fast convergence are listed in Table 3. In each random walk step the parameters are randomly altered in an arbitrary way. In the case of our algorithm, the parameters are multiplied by a log-normally distributed random number, M_p, with location $\mu = 1$ and the scale parameter σ_p, making sure that the multiplicator is always positive and close to 1,

$$M_p \sim \ln\mathcal{N}(\mu = 1, \sigma_p), \tag{9}$$

where p indexes the fitting parameter. The values of σ_p for each parameter taken in our algorithm are listed in the Table 3.

In order to convert the drawn voxels to electron density, we use a scaling function and add noise

$$\varrho_{drawn} = (\varrho_{Fe} - \varrho_{CF}) \cdot I + \varrho_{CF} + \text{noise}, \quad \text{noise} \sim \mathcal{N}(\mu = 0, \text{rms}), \tag{10}$$

where ϱ_{drawn} is the resulting electron density of a given drawn voxel, ϱ_{Fe}, ϱ_{CF} are the electron density of iron and carbon fiber, respectively, I is the value of a drawn voxel. A histogram of one range of depths $(x - \Delta x/2, x + \Delta x/2)$ is fitted at a time, where $\Delta x = 20$ nm is the depth bin width. In each step all the simulation parameters are altered. The new set of parameters is accepted if an optimization function returns a lower value than the previous one. The optimization function is defined as

$$\text{opt} = \frac{\sum_k \left((H_e(k) - H_s(k))^2 \cdot (H_e(k))^{-1} \right)}{\sum_k (H_e(k))^{-1}}, \tag{11}$$

where $H_e(k)$ and $H_s(k)$ are the experimental and simulated histogram bins, respectively, of the k-th electron density. The optimization function has a meaning of a weighted average of squares of deviations of a simulated histogram from an experimental histogram, where the weights are equal to the inverse of the number of counts of the k-th bin of the experimental histogram. The weights were chosen in such a way in order to account for the expected dispersion of the number of counts. It is known that if the measurement points are not correlated, the fitting procedure minimizes the uncertainty of the parameter estimators when the weights are defined as inverses of variances of each measurement. It is assumed that the distribution of counts is Poissonian with mean equal to variance and defined as λ. Therefore, since the number of counts $H_e(k)$ is a good estimate of λ, the choice of weights $\lambda^{-1} \approx (H_e(k))^{-1}$ is justified. Only the bins with non-zero number of counts at both histograms are taken into the convergence evaluation to avoid division by zero. The convergence criterion is arbitrary and we have defined it as opt$<10^{-4}$, which has given a satisfactory convergence of the histograms.

3.7. Results and discussion of nanoparticle abundance assessment from PXCT data

Fig. 8 presents an example of histogram fitting results for the depth range between 110 nm and 130 nm, where the electron density shoulder is the most pronounced.

The fitting procedure has been repeated 50 times in order to get the statistical measure of an error. Fig. 8a shows an experimental histogram along with the simulated histogram, whereas Fig. 8b

Table 3
Simulation parameters that undergo random walk, their initial values and scale parameters σ_p of a log-normally distributed random variable that multiplies the parameters in each iteration.

Parameter p	Initial value	σ_p of step
ϱ_{CF}	0.5 Å^{-3}	2.0×10^{-3}
rms	0.025 Å^{-3}	1.0×10^{-2}
f	$\propto \exp(-v/3)$	3.5×10^{-1}

presents the corresponding fitted NP volume distribution f. Both fitted curves represent the geometric mean, whereas the 95% confidence intervals in both cases represent a double geometric standard deviation, namely,

$$U, D = \exp\left(\overline{\log X} \pm 2\sqrt{\overline{\left(\log X - \overline{\log X}\right)^2}}\right), \tag{12}$$

where X is the sample element, U and D are the upper and lower bounds of the confidence interval, respectively, whereas the bar represents a mean value. Geometric statistics has been chosen, since it is more representative for the data on logarithmic scale. In Fig. 8a the lower histogram bins appear to have a greater spread. On a logarithmic scale the magnitude of spread corresponds to the relative error of measurement. It remains in agreement with the assumption of Poissonian-distributed number of bin counts, which has a relative error equal to the inverse of the square root of number of counts. Fig. 9 shows the full distribution $f(x, v)$ of iron NPs.

It can be seen that at large depths there is a sharp peak at volume $v \approx 0$. It is expected, because it corresponds to a vast dominance of pure carbon fiber material and it means that barely any NPs of any size are detected at depths larger than 300 nm. At the range of depths from 75 nm to 125 nm however, there appears an island of iron NPs of volumes ~3.5 × 10^4 nm^3, corresponding to a diameter of 40 nm, whereas in other regions NPs of smaller diameter dominate. This result is in good agreement with SEM measurements, one of them shown in Fig. 1, where the NP size has been determined to fall within a range between 20 nm and 40 nm. This agreement indicates that the methodology applied for the NP distribution assessment is accurate.

Fig. 10 shows a graph of the iron atomic concentration versus depth into the CF calculated using equation (7). Error bars represent a double standard deviation. From the graph it is clear that there is a measurable amount of iron below the surface of CF. The concentration curve is a peak curve with the center at about 100 nm below the CF surface and width of about 150 nm, which is considerably larger than the resolution. Therefore it can be reasoned that the NPs have penetrated the CF significantly during the CNT growth processing. The iron film thickness equivalent to the amount of iron detected within the fiber volume has been evaluated using equation (8), obtaining a value $t = 5.42 \pm 0.31$ Å. It constitutes a significant fraction of the 5 nm-thick sputtered film (greater than 10%), especially taking into account that the 5 nm is merely a peak value, as the sputtering - being a field-of-view coating technique - has been performed only from two sides of a fiber and the actual sputtered thickness averaged over the CF surface is smaller. It means that not only does the iron cause defects penetrating into the CF, but also the penetration itself depletes the total amount of iron that should have been physically accessible on

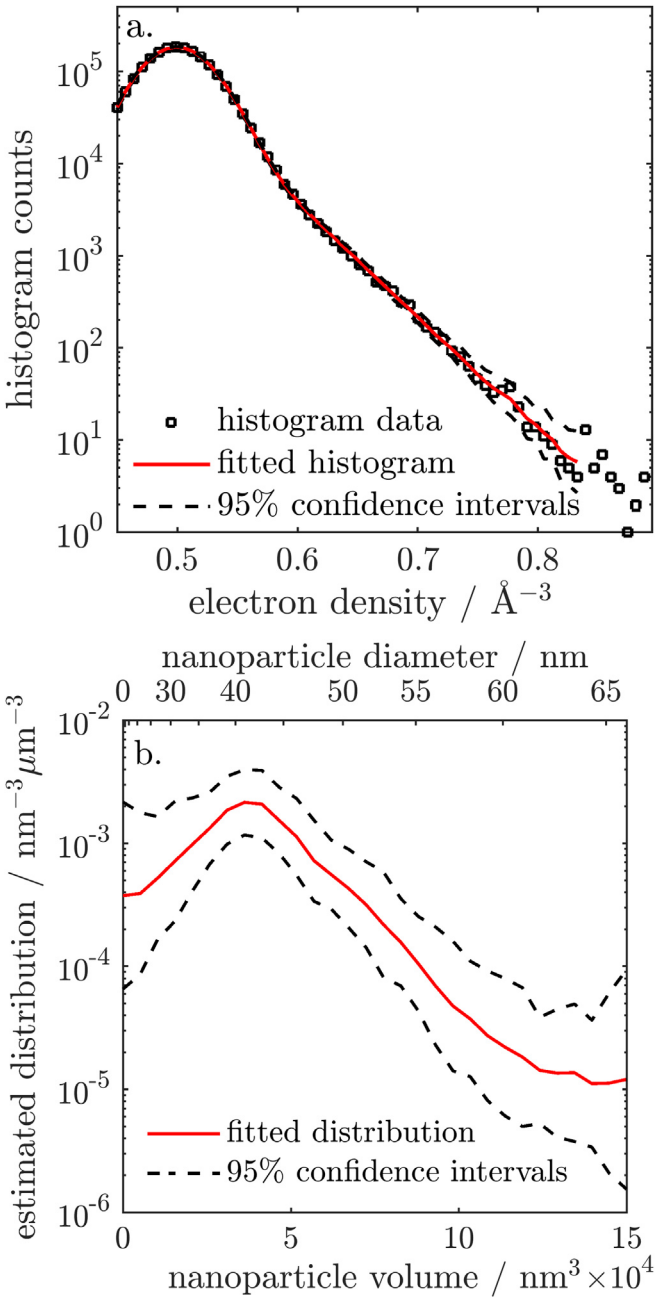

Fig. 8. The result of the fitting procedure; (a) experimental histogram of electron density voxels in the range between 110 nm and 130 nm (black open squares) and the simulated curve (red solid line); (b) the corresponding NP volume distribution (red solid line). A NP diameter axis corresponding to the volume axis is added at the top of the graph. In both cases, the black dashed lines stand for the 95% confidence intervals. (A colour version of this figure can be viewed online.)

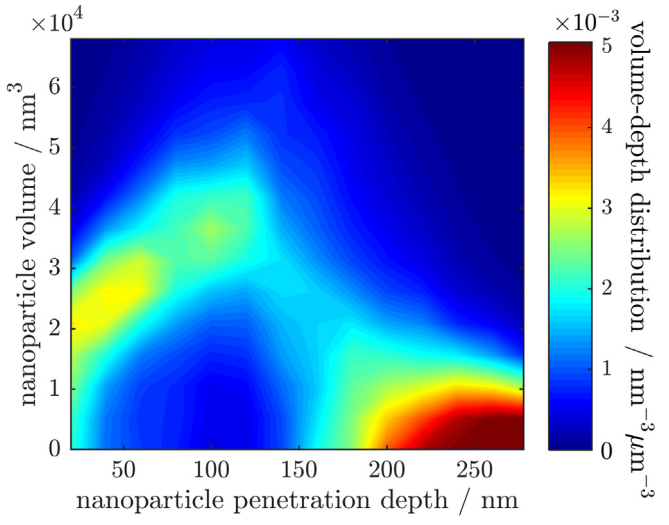

Fig. 9. Iron NP distribution with respect to NP volume and depth into the CF from PXCT data analysis. The 2D distribution describes number of NPs per nm^3 of NP volume and per μm^3 of the sample volume. The position of the peak of the distribution is visibly elevated at depths around 100 nm, which reflects the presence of NPs of largest size in this region. Color coding reaches values up to 5 × 10^{-3} nm^{-3}μm^{-3} to emphasize the relevant features. (A colour version of this figure can be viewed online.)

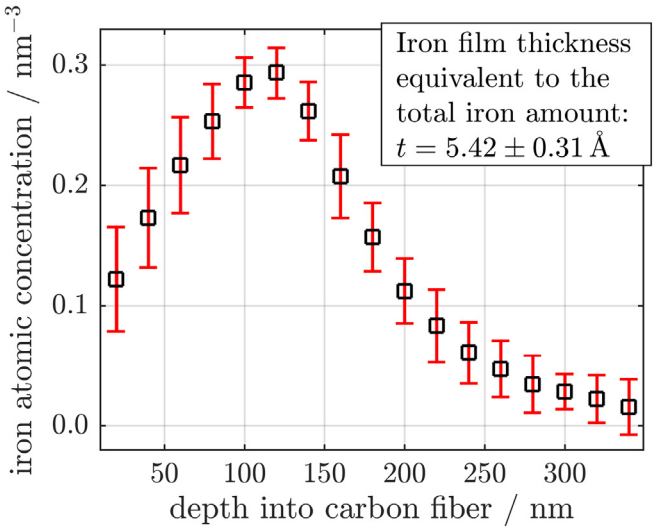

Fig. 10. Iron atomic concentration versus depth into the CF calculated from the distribution of iron NPs estimated from data extracted from PXCT. (A colour version of this figure can be viewed online.)

the surface for CNT growth and, effectively, the growth efficiency may decrease.

The observation of iron NPs within the fiber indeed proves the hypothesis that the NP volumetric diffusion occurs during a direct growth of CNTs. However, it also raises a question why such a phenomenon occurs. It does not seem to be a typical diffusion of iron within the carbon fiber, because the material of the NPs seems to be localized instead of being diffusively blurred. Therefore we hypothesize that the fundamental mechanism of the phenomenon is the carbon diffusion within iron that drives the NP transport within the carbonaceous body of the fiber. This is supported by the fact that carbon is soluble in iron and volumetric carbon diffusion through a metallic NP is a crucial element of both tip- and root growth of multiwall CNTs [32]. It has been observed that the choice of different catalyst systems such as Fe-Cu [8] or Fe-Ni [9] mixtures instead of pure iron minimizes the etching into carbon. We believe that the methodology of data analysis introduced in this work allows for a direct quantitative assessment of the etching in the mentioned systems as well as in the ones that will be developed in the future. It can lead to a better fundamental understanding of the process and provides a new insight into the process optimization.

3.8. Validation of PXCT data analysis results by means of scanning transmission electron microscopy and energy-dispersive X-ray spectroscopy

The results of PXCT imaging data analysis were cross-checked with STEM and EDX. Both have been carried out in the Helios NanoLab™ 650 FIB/SEM. Slices of CF samples of ~100 nm thickness prepared by FIB cutting were examined. The two critical samples were analyzed: the unprotected- and 11 nm-alumina-protected CF.

STEM examination has been conducted to confirm the conclusions from PXCT. Bright field (BF) images at 30 kV electron acceleration voltage have revealed the positions and shapes of NPs by reduced intensity, see Fig. 11. The resolution of STEM was much higher than that of PXCT and the edges of NPs are resolved, therefore a straightforward image analysis can be applied. From the STEM images it is clearly seen, that the iron nanoparticles are indeed localized instead of being diffusively blurred, which supports the hypothesis of diffusion of iron NPs driven by carbon diffusion through a NP. In the case of the unprotected CF, the NPs were present both below and over the CF surface in the CNTs, see Fig. 11a. As expected, the protected CF sample exhibited no presence of NPs below its surface, only above it within the grown CNTs, which remains in agreement with the PXCT results, see Fig. 11b.

Furthermore, the two-dimensional volume-penetration depth distribution has been estimated form the STEM data, see Fig. 12. The particle sizes have been extracted using ImageJ software with a built-in particle analysis tool. Prior to particle analysis, the image has been processed in ImageJ with background subtraction and thresholding. As a result, the algorithm returns particle areas. In the further analysis it is assumed, that the NPs are spherical. Due to a low number of particles available for analysis, the distribution has been estimated using a kernel probability density estimation function ksdensity() based on the method described in Ref. [33] available in MATLAB and Statistics and Machine Learning Toolbox Release 2016b, The MathWorks, Inc., Natick, Massachusetts, United States. The default smoothing parameter was chosen, being proven to be optimum for normal distributions. Compared to the analogous distribution extracted from PXCT (Fig. 9), a main difference is the appearance of a high peak at volume ~10^4 nm^3 and depth ~75 nm. This volume corresponds to NP diameter of ~25 nm, which is half of the resolution of PXCT. It can be explained by the fact, that in this region of depths the concentration of small NPs gets very

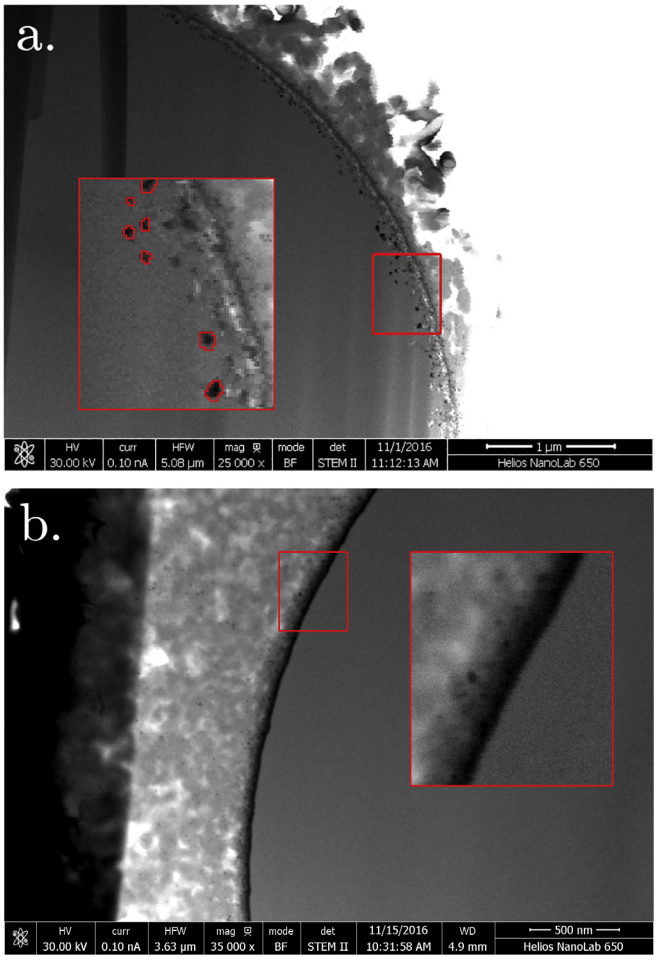

Fig. 11. Thin BF STEM images performed on thin CF slices; (a) unprotected fiber; (b) 11 nm-alumina protected fiber. We can observe spots of reduced intensity, which correspond to iron NPs. The insets show magnifications of the relevant regions; additionally, edges of NPs are shown as extracted using ImageJ, several NPs were ignored because of ambiguity due to of overlapping or low contrast. (A colour version of this figure can be viewed online.)

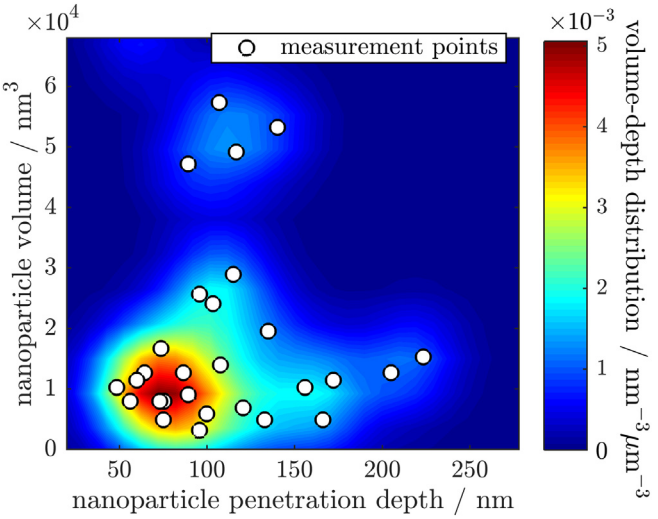

Fig. 12. Nanoparticle volume-penetration depth measurement points from STEM image analysis for the unprotected CF (white filled circles) and the corresponding distribution approximated using two-dimensional kernel density estimation (colorful contour plot); for comparison with Fig. 9. (A colour version of this figure can be viewed online.)

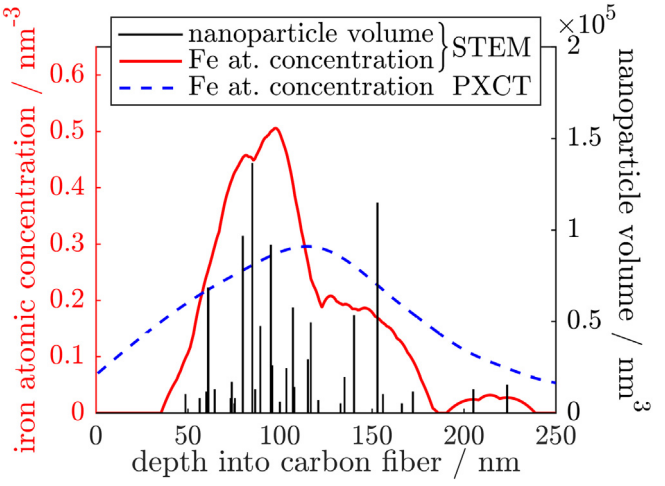

Fig. 13. NP volume obtained from STEM image analysis (black solid bars), iron atomic concentration evaluated from NP volume from STEM data assuming spherical NPs (red solid line) and iron atomic concentration extracted from PXCT data for the purpose of comparison (blue dashed line). All data are plotted as a function of the depth into the CF. (A colour version of this figure can be viewed online.)

large, as seen in STEM images (Fig. 11a) and there is a high chance that multiple NPs fall as close together as PXCT resolution. Therefore the NP agglomerates could have been interpreted by the 3D image analysis as a lower quantity of larger NPs. This phenomenon constitutes a limitation of the 3D image analysis methodology developed in this work, as the algorithm assumes that NPs are well separated from each other, however it does not significantly alter the total amount of iron estimated as a result. This statement is supported by simulations, as discussed in Appendix F.

The iron atomic concentration versus depth has been numerically evaluated from the NP volume-position data, see Fig. 13.

Numerical integration assumed spherical shapes of iron NPs and an average CF slice thickness of approximately 100 nm. The data extracted from PXCT is shown for comparison. The agreement is well pronounced. The positions of the peak of iron concentration are very close and the decay with increasing depth behaves similarly. The spread of the distribution from PXCT is noticeably larger, however it can correspond to the NP position uncertainty originating from the 50 nm resolution of PXCT. The differences between the two curves of iron atomic concentration may also arise from a vast discrepancy of statistical sampling between the two methods. The PXCT analysis has been carried out on ~8.2 μm long CF, whereas the STEM only on a ~100 nm thick CF slice. Moreover, the thickness of CF slice for STEM is already of the order of magnitude of the NP size, therefore a substantial number of NPs could have been cut with a FIB effectively exhibiting a smaller diameter than prior to processing.

EDX has been conducted to examine the elemental composition of the specific nanoscale features of the samples. The results are treated qualitatively, because quantification is substantially sensitive to a precise knowledge of the geometry that is not available in this study. Nonetheless, the results provide the information critical to confirm the conclusions obtained with the PXCT analysis. In the case of the unprotected CF, EDX has been carried out on three regions of interest (ROIs): the inside of the fiber (control) and on two iron NPs below the surface. The largest NPs found in the SEM image were examined (diameters 53 ± 2 nm and 40 ± 2 nm of nanoparticle 1 and 2, respectively, see Fig. E 1 in Appendix E). In the case of the protected CF, two ROIs were examined: the inside of the fiber (control), and alumina film with no NPs. For EDX a 3 kV acceleration voltage was chosen, which allowed to examine all the relevant elements present in the samples. The examination has revealed that the NPs are indeed composed of iron and also partially of oxygen. This is concluded from the increased intensity of the iron and oxygen peaks for the case of ROIs with NPs in reference to the control, see Fig. 14a. Since the CNT growth has been carried out in a reducing hydrogen atmosphere and the NPs are well-embedded within the CF or CNTs, it is possible that iron got oxidized in the ambient atmosphere after the FIB cut. As expected, the ROI of the CF with a protective alumina film exhibits elevated intensities of aluminum and oxygen peaks, see Fig. 14b. We note that the EDX measurements on these ROIs caused a change in the appearance of these regions in the SEM image in Fig. E 1. This observation is discussed in Appendix E.

3.9. Comparison between the PXCT and the FIB/STEM/EDX approaches

We have successfully verified the results and conclusions of PXCT data analysis by FIB/STEM/EDX investigation. It was only possible thanks to the advantages of the latter approach. The first one is the possibility of direct identification of elements as opposed to PXCT, which identifies only average local electron density. The other advantages are a high resolution down to several nanometers as compared to 50 nm resolution of PXCT and the relatively high availability of the equipment, as PXCT is performed on synchrotrons. On the other hand, using PXCT has enabled us to obtain data of a high statistical content non-destructively, coming from a large uninterrupted volume of CF that is not possible to probe with the other approach. The other reason for us to use PXCT was the simplicity of sample preparation. Furthermore, we have developed an algorithm that is able to overcome the limitations of the resolution of the PXCT method to a great extent.

From our experience, we recommend using PXCT on microfibers when a large volume of the fiber should be analyzed, when a destructive method is unacceptable and especially when the interesting features of the samples are at a scale of more than the PXCT resolution. Alternatively, we would recommend the FIB/STEM/EDX approach in the cases when a low information volume is satisfactory, when elemental analysis is crucial and if the high

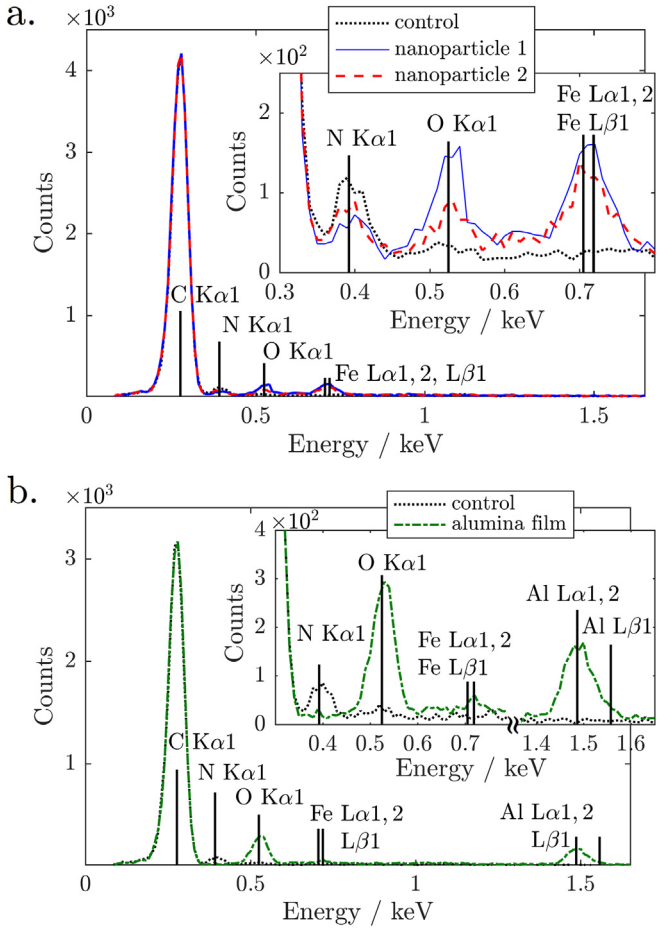

Fig. 14. EDX spectra of the (a) unprotected and (b) 11 nm alumina protected CF at different ROIs: control (black dotted line), nanoparticle 1 (blue solid line), nanoparticle 2 (red dashed line), alumina layer (green dash-dotted line). The nominal positions of X-ray emission peaks are indicated by vertical solid black lines. The insets show magnifications of the most relevant peaks. The positions of ROIs corresponding to the spectra in the graph (a) are indicated in Fig. E 1 in Appendix E. (A colour version of this figure can be viewed online.)

resolution is required to resolve fine features of the sample.

4. Summary and conclusion

In this work we introduce a methodology for the assessment of iron NP size distribution within CFs based on electron density histograms and successfully apply it. The methodology relies on a self-consistent algorithm overcoming the obstacle that the NPs are not resolved in the measurement, which might be useful in other studies of features of size below the measurement resolution. The data analysis shows that, in the case of the unprotected carbon fiber, NPs of diameter around 40 nm are present at a depth of about 100 nm below the fiber surface. In the case of a CF protected with an 11 nm alumina film prior to growth, we do not observe any presence of iron below the fiber surface. We have verified the conclusions of PXCT imaging and data analysis conducting STEM and EDX examination, which provided a substantial reassurance both on the PXCT results and on the novel 3D image analysis methodology. Therefore, in this work we confirm that such an ultrathin film constitutes a sufficient barrier against iron infiltration in the growth process of CNTs on CF, effectively blocking the further defect formation. This explains the preservation of mechanical strength observed in our recent study [12]. The data analysis methodology can be applied to evaluate the efficiency of other etching-preventing solutions such as the ones introduced in Refs. [8] [9], or in future methods. We state a hypothesis that the transport of NPs within the bulk of CFs is driven by diffusion of carbon through each NP, which is why the NPs retain the integrity instead of getting diffusively dissolved in the body of CF. The results obtained improve the understanding of the mechanical properties of carbon fibers after processing and constitute a significant step in the development of hierarchical composites.

Acknowledgements

We would like to thank Dr. Manuel Guizar-Sicairos from the Paul Scherrer Institute for discussions and sharing his expertise in the resolution-limiting effects occurring in PXCT imaging. We would also like to thank the crew of Nano Imaging Lab at University of Basel for consultation on the strategy for the verification of the PXCT results, especially Daniel Mathys with whom the FIB/STEM/EDX examination has been carried out. We also acknowledge the Swiss Nanoscience Institute at University of Basel for funding this research (SNI PhD project P1402).

Appendix A. Sample preparation details

Initially, the CFs were coated with alumina films using ALD, which is a thin film fabrication technique that allows for extremely uniform coating of outer surfaces of samples of virtually any geometric complexity while guaranteeing an atomic precision in layer thickness control. This feature of the method makes it ideal for a uniform and conformal coating of a CF with a barrier film. Alumina has been chosen as the coating material as it is a popular support for CNT growth [32]. The samples have undergone a 10-min ultra violet/ozone treatment before the ALD coating. The coating has been carried out using a commercial ALD system Savannah 100 (Cambridge NanoTech, UK). The precursors for alumina ALD process were trimethyl aluminum (TMA) and deionized water. The process temperature has been set to 225 °C. In our previous study the ALD growth rate of alumina film has been calibrated by means of ellipsometry of a silicon wafer coated simultaneously alongside the CF in the ALD reactor. In the present study we are investigating the protective effect of the 11 nm-thick alumina film against the iron NP diffusion. Additionally, a film of 500 nm thickness is examined being well above the 50 nm resolution of the images obtained in this study.

The CVD growth of CNTs on a solid substrate requires delivery of a metal catalyst on the surface, typically iron. In this study, the surfaces of fibers have been coated with iron catalyst thin film using magnetron sputtering. In this method, metal is physically vaporized from a target using an electron beam in vacuum. The surface of the sample in the reactor is coated with the metal. The reactor chamber pressure during depositions was 1.2×10^{-5} mbar. The reactor was kept at room temperature. The deposition rate was measured by a quartz balance and was set to 0.5 Å s^{-1}. The deposition rate was controlled by adjusting the acceleration voltage of the electron beam prior to opening the shutter. The deposition was terminated at 5 nm film thickness by closing the shutter. The fibers were coated from two opposite sides in separate processes in order to partially overcome the shadowing effect of the technique.

After the sputtering of the catalyst, the CNT growth was carried out. The CNTs were grown on the samples in a custom atmospheric pressure CVD reactor. The samples of carbon fiber were put into a 136 mm diameter quartz tube of the CVD oven. The process time was 15 min. The growth has been carried out at a 750 °C temperature. The gases used in the process were ethylene and hydrogen. The volumetric flow rate of each gas was 1 l min^{-1}. At this stage of

the process, the sputtered iron film gets reduced by hydrogen and undergoes transformation into metallic NPs, such that the CNT growth can be initiated and continued.

Ultimately, four different samples were prepared for the further examination. One pristine CF without any further treatment was taken as a control. The second sample was sputtered with an iron catalyst film of 5 nm nominal thickness and CNT growth was carried out on it. Another two CFs were prepared with a protective alumina layer of 11 nm and 500 nm thickness, respectively, prior to catalyst sputtering and subsequent CNT growth.

Appendix B. Mechanical properties of the treated fibers – single fiber tensile testing.

In this study we refer to the mechanical performance of the fibers examined in our previous work [12]. We have investigated the influence of the thickness of the ALD alumina film necessary to apply prior to CVD processing in order to retain the tensile strength of a CF. For the convenience of the reader we show these results here in a condensed form.

We have tested the influence of two factors on the fiber strength at varying thickness of the alumina film: fiber prestraining by 0.2% and CVD CNT growth process equivalent to the one carried out in this work. The results are summarized in Fig. B 1.

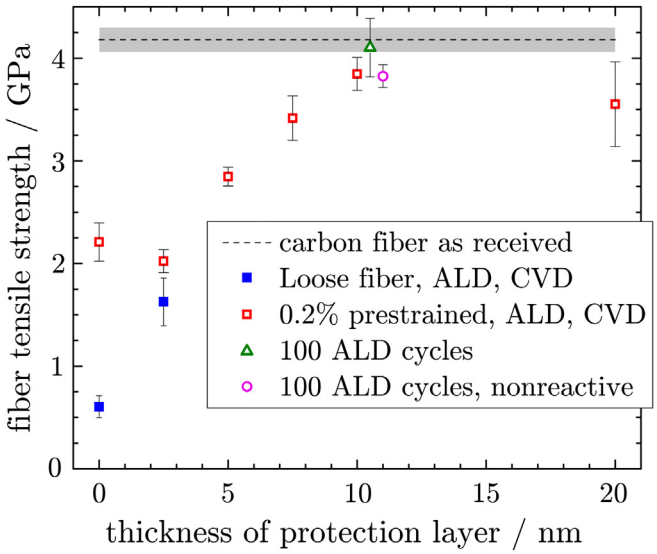

Fig. B 1. Summary of the tensile test results carried out in our recent work [12]: dashed black line with grey bar represents the baseline strength of the AS4 fiber as received along with the error interval; closed blue squares – loose (not prestrained) CF having undergone ALD and CVD processes; open red squares – 0.2%-prestrained CF having undergone ALD and CVD processes, open green triangle – CF after ALD with no further processing (the number 100 refers to the number of ALD cycles); open violet circle – CF having undergone 100 ALD cycles and thermal treatment at 750 °C CVD temperature in argon, but with no presence of a catalyst or reactive gas. The latter two points are offset along the horizontal axis for clarity. Thickness of oxide layer equal 0 nm refers to no ALD processing for the given sample.

We have observed that the prestrain is a crucial factor in retaining the CF strength in the process. Furthermore, we have concluded that the optimum alumina film thickness is about 11 nm and its further increase is not beneficial.

Appendix C. Experimental details of ptychographic X-ray computed tomography measurements

The coherent X-ray illumination onto the sample was defined by a Fresnel zone plate made of Au [34] with 150 μm diameter and 60 nm outer-most zone width, resulting in a focal length of 52.82 mm at the X-ray photon energy of 7.00 keV which was used in the experiment. We estimate that a flux of about 6.4×10^8 photons/s was delivered by the Fresnel zone plate. The sample was placed 1 mm downstream the focus in such a way that the size of the beam on the sample was about 3 μm. Coherent diffraction patterns were recorded from the specimen in transmission geometry at different positions of the sample following the pattern of a Fermat spiral [35] with an average spacing between scanning points of about 0.8 μm. Diffraction patterns were recorded with a Pilatus 2 M detector with 172 mm pixel size [36] placed at 7.355 m from the sample with an acquisition time of 0.1 s for each diffraction pattern. We thus estimate a flux density of 1.2×10^8 photons/μm^2 incident on the specimen for each ptychographic scan. Ptychographic scans were acquired at different angles of the specimen with respect to the incoming beam in equal angular steps between 0 and 180°. Due to the inactive areas of the detector in the gaps between modules, the detector was traslated in both directions perpendicular to the beam propagation direction alternating between two positions at consecutive angular steps. In the ptychographic reconstructions, each pair of consecutive scans were reconstructed together, such that two images were obtained while sharing the same illumination probe, as explained in Ref. [37] and introduced for tomographic acquisitions in Ref. [17].

Appendix D. FIB cutting procedure

Helios NanoLab™ 650 is equipped with gallium ion gun, field-emission electron gun, nanomanipulator Omniprobe 200 produced by Oxford Instruments, EDAX X-ray detector produced by Oxford Instruments and gas injection system for focused-ion-beam-induced deposition (FIBID) of platinum for precise welding at nanoscale.

Initially, fibers were mounted horizontally on SEM stubs by a conductive carbon tape and additionally welded with a silver paint for increased conductivity and stability. Care was taken to keep the ends of fibers loose for convenient further nanomanipulation. The stage was moved to a eucentric position in which is the sample plane was perpendicular to the ion beam and in an optimum working distance with respect to the electron beam being ~4 nm. In such a configuration, ion beam milling is performed perpendicularly to the fiber axis and the process can be monitored in-situ by sequential SEM imaging.

The procedure began with cutting off the loose part of the fiber, see Fig. D 1a. After that, a nanomanipulator needle approached the fiber end from a side and was welded to it by platinum FIBID, see Fig. D 1b. Subsequently, fiber was cut above the welded point resulting in ~500 nm thick CF slice, see Fig. D 1c. The cutting was performed with 30 kV ion acceleration voltage and relatively high current in the range of 0.79–2.5 nA. The rectangle scan was chosen as the scanning strategy for cutting. Final polishing of the sample was then performed from both sides of each slice in order to obtain the desired thickness and to get rid of the most of gallium redeposition that could obscure the results, see Fig. D 1d. The polishing was performed at the same acceleration voltage of 30 kV, but at a smaller current within the range of 70–200 pA in order to obtain a smooth, well-defined surface of limited gallium contamination. The scanning strategy for polishing was a sequential line scan gradually proceeding towards the desired slice surface. It was ensured, that the scan line proceeded to a new position after it had already successfully milled away its target.

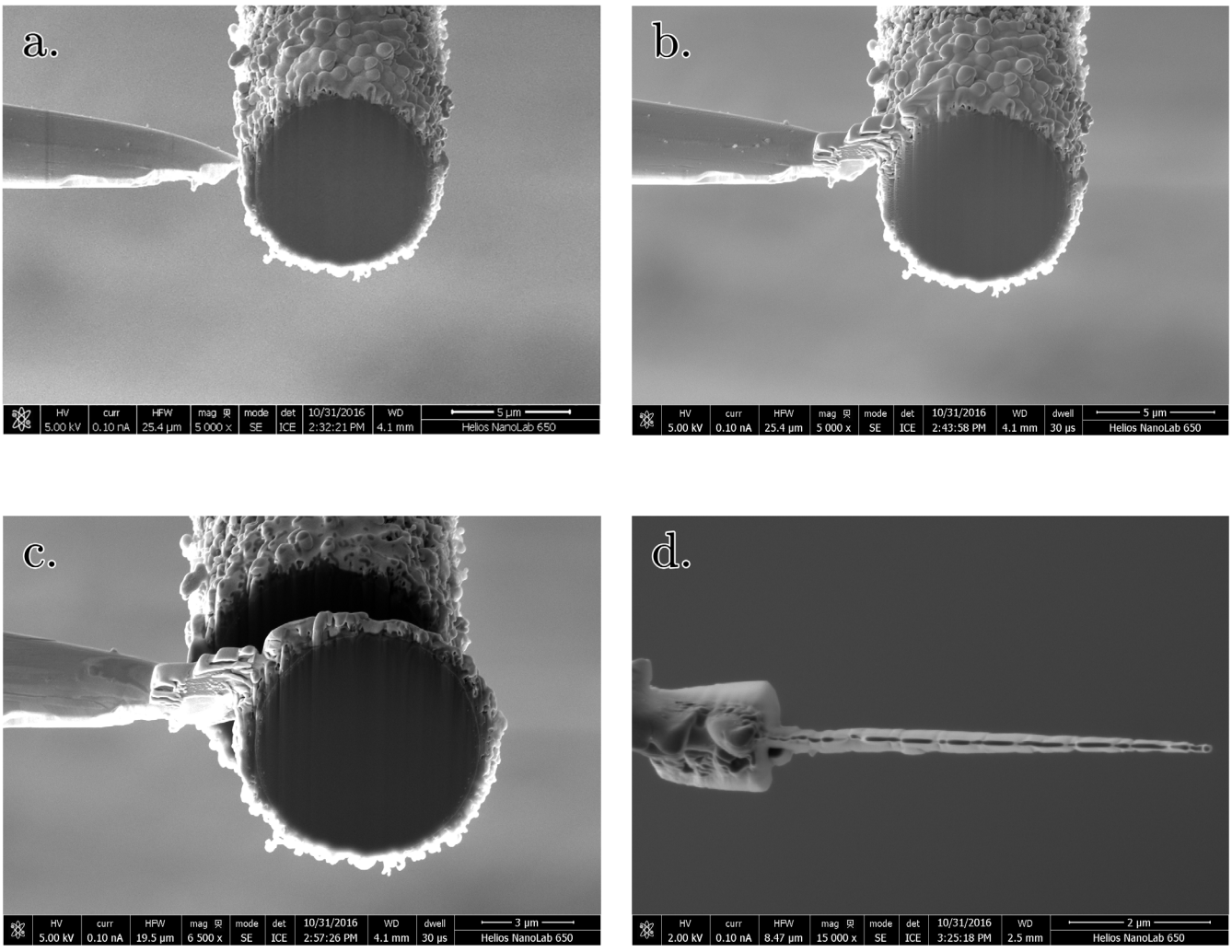

Fig. D 1. SEM images of subsequent steps of FIB cutting procedure of CF slices; (a) loose-end of the fiber cut off; (b) nanomanipulator needle welded to CF using focused-ion-beam-deposited platinum; c. relatively thick CF slice cut off; (d) thin CF slice after polishing (top view).

Appendix E. Influence of electron beam irradiation during EDX on secondary electron image

As mentioned in the main part of this work, the areas irradiated with electron beam during EDX have changed their appearance on secondary electron image. Within an irradiated ROI, the area of NP has increased intensity appearing brighter in the image, whereas the surrounding carbon has a decreased intensity, appearing darker, see Fig. E 1.

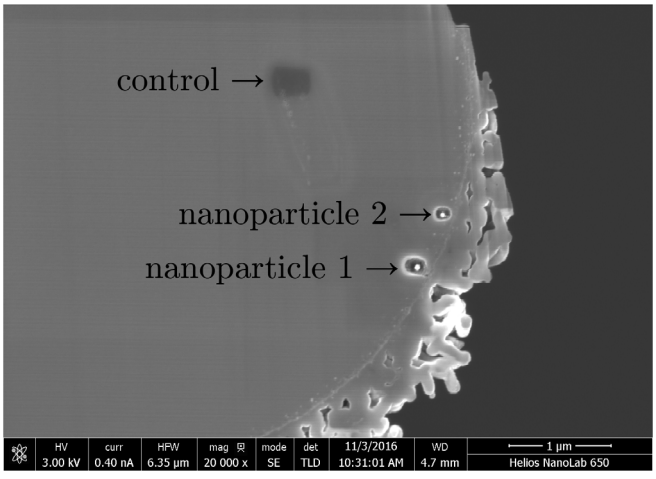

Fig. E 1. SEM of the unprotected CF slice examined by EDX. Labels correspond to the spectra in Fig. 14a.

The observations can be explained by the following phenomena. The well-known local deposition of amorphous carbon by electron beam from free hydrocarbons present in the non-perfect vacuum within the SEM chamber may have caused the local darkening of the secondary electron image of CF. The other phenomena is the catalytic action of iron triggered by local heating by 3 keV electron beam. It could have resulted in diffusion of NP towards the surface and precipitation of carbon electron beam causing the apparent brightening of the NP. The confirmation of the hypothesis however requires an additional study of the interaction of iron NPs with the surrounding carbon upon electron beam irradiation, which lies beyond the scope of this work.

Appendix F. Influence of small nanoparticle separation on the results of PXCT data analysis

In section 3.8 of this work, which is devoted to the verification of PXCT data analysis by means of FIB/STEM/EDX examination, we have pointed out that due to the high chance of NPs getting close together comparable to the spatial resolution obtained in PXCT, there is a possibility that multiple smaller NPs can be interpreted as a lower number of larger NPs. However, we stated that it does not induce a significant error in the resulting estimate of iron content in a given region. In this section we support this statement by an example simulation of two NPs getting close together and its subsequent analysis employing an algorithm analogous to the one introduced in section 3.6. For the sake of simplicity, in the simulation we assumed an electron density for CF of $\varrho_{CF} = 0.5\ \text{Å}^{-3}$ and an isotropic Gaussian PSF of $\sigma = 29$ nm, which falls between the radial σ_r and the axial σ_z obtained from the analysis. We defined two NPs of diameters of 29 nm and 23 nm being not greater than σ. Blurring of NPs of diameter not greater than σ with PSF produces electron density images very well-described with a Gaussian

$$\varrho(\mathbf{r}) = \varrho_{CF} + \frac{N_e}{\left(\sqrt{2\pi}\,\sigma\right)^3} \exp\left(- \frac{|\mathbf{r} - \mathbf{r}_0|^2}{2\sigma^2} \right), \tag{13}$$

where ϱ is the simulated electron density image, $\mathbf{r}$ is a position vector, $\mathbf{r}_0$ is the position of the center of the NP, N_e is the total number of electrons in the NP. N_e can be calculated as

$$N_e = \frac{Z_{Fe} d_{Fe} V_{NP} N_A}{\mu_{Fe}}, \tag{14}$$

where V_{NP} is a volume of the NP, Z_{Fe}, is the atomic number of iron, d_{Fe} is iron mass density and μ_{Fe} is the molar mass of iron. This means that at this NP size all the information about any specific shape is lost and the NPs can be defined as a 3D Dirac delta functions multiplied by the corresponding N_e. We took advantage of this fact to produce the simplified simulation. In the simulation, 40 evenly distributed values for distances between NPs were considered ranging from 0 nm, meaning a complete coalescence of the NPs, up to 116 nm. The cross sections of the produced images at 6 values for the NP separation are shown in Fig. F 1. We can already see that at a distance of 46 nm it is no longer possible to identify the two NPs.

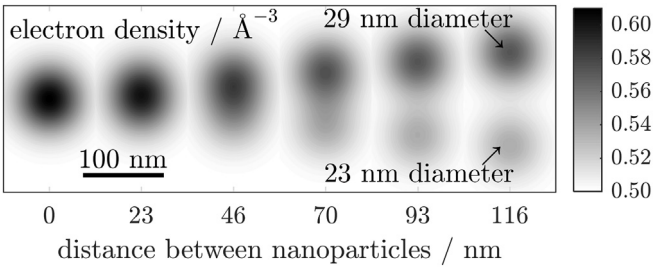

Fig. F 1. Cross sections of simulated electron density images produced by two NPs of different diameters (indicated by arrows) at 6 distances.

The subsequent analysis has been carried out employing a methodology introduced in section 3.6 with minor changes. Instead of artificially adding Gaussian noise to the electron density maps, their histograms were numerically convolved with a Gaussian of rms = 0.029 Å^{-3} being close to the experimental one. Such an operation is mathematically equivalent to adding noise, but it does not introduce noise at low histogram bins and the histograms remain smooth. Consequently, the fitting procedure does not have to account for the noise and the optimization function can be defined as

$$\text{opt} = \frac{1}{N} \sum_{k=1}^{N} \log^2 \left(\frac{H_e(k)}{H_s(k)} \right), \tag{15}$$

where H_e is the input histogram obtained from the simulated electron density map of the two NPs at proximity, whereas H_s is the histogram being a result of a linear combination of histograms of well-separated NPs of different volumes, in this version of the algorithm ranging from 0 to 2.1×10^4 nm. The optimization function (15) represents a non-weighted mean square deviation at logarithmic scale. The usage of such an optimization function is justified by the fact that the algorithm should be sensitive to the features of the histograms that become apparent at the logarithmic scale. The fitting termination criterion was set as opt<5×10^{-3} which has given excellent fitting results. A one-dimensional NP volume distribution $f(v)$ was set as a fitting parameter.

The resulting NP volume distribution is shown in Fig. F 2. It is well-pronounced, that at distance greater than 100 nm being about 3.5σ, the NPs are well distinguished by the algorithm. However, as the distance decreases, the algorithm interprets the image as if the smaller NP was getting gradually larger, but its contribution to the final histogram was decreasing. On the other hand, the bigger NP contribution gradually intensifies. It continues until the distance of ~60 nm is reached, which corresponds to about 2σ. At this stage, the apparent contribution of the smaller NPs vanishes completely. With the further decrease of distance, the image is interpreted by the algorithm as if one NP was increasing in volume, but decreasing slightly in contribution to the histogram. Ultimately, at the distance equal 0 the output shows clearly one NP of a volume equal the sum of the two.

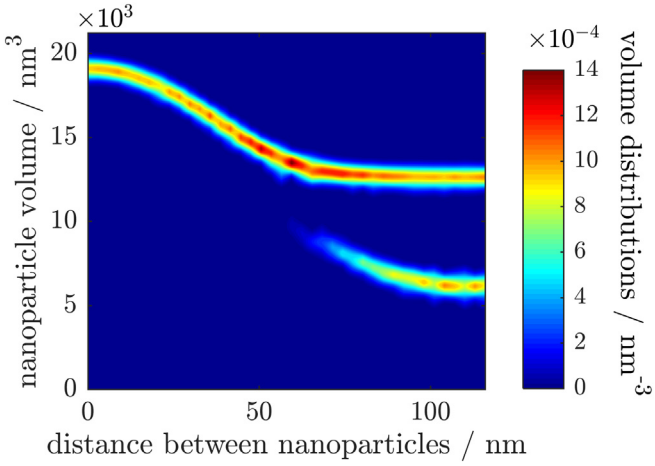

Fig. F 2. Output NP volume distributions versus distance between the two NPs. An artifact of a peak at zero NP volume has been erased for clarity.

Using the output $f(v)$, the total iron volume V_{Fe} can be calculated as

$$V_{Fe} = \int_0^{v_{max}} v f(v) dv, \tag{16}$$

which can be compared with the expected total iron volume being the sum of the two NP volumes. The relative error of the evaluated total iron volume is presented in Fig. F 3. We observe that the greatest error that is encountered is only about 6.5%, therefore we claim that it is not significant.

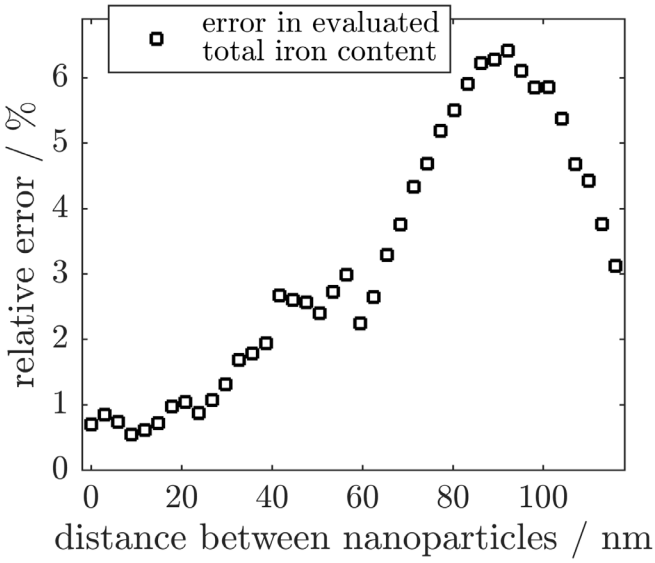

Fig. F 3. Relative error in the total iron content evaluated using the methodology introduced in this work in the simulated case of two NPs separated by distances comparable to the PXCT resolution.

The results of this simulation constitute an example that, in case of close proximity between NPs, the introduced algorithm might mistake several NPs as one or misjudge the proportions of the NP sizes. Nonetheless, the simulation results exemplify that in such a case the algorithm does not introduce a significant error in the estimated total iron content.

References

[1] H. Qian, E.S. Greenhalgh, M.S.P. Shaffer, A. Bismarck, J. Mater. Chem. 20 (23) (2010) 4751, http://dx.doi.org/10.1039/c000041h.
[2] J.W. Johnson, D.J. Thorne, Carbon 7 (6) (1969) 659–661, http://dx.doi.org/10.1016/0008-6223(69)90520-X.
[3] H. Qian, A. Bismarck, E.S. Greenhalgh, G. Kalinka, M.S.P. Shaffer, Chem. Mater. 20 (5) (2008) 1862–1869, http://dx.doi.org/10.1021/cm702782j.
[4] H. Qian, A. Bismarck, E.S. Greenhalgh, M.S.P. Shaffer, Compos. Part Appl. Sci. Manuf. 41 (9) (2010) 1107–1114, http://dx.doi.org/10.1016/j.compositesa.2010.04.004.
[5] S. Zhu, C.-H. Su, S.L. Lehoczky, I. Muntele, D. Ila, Diam. Relat. Mater. 12 (10–1) (2003) 1825–1828, http://dx.doi.org/10.1016/S0925-9635(03)00205-X.
[6] N. Sonoyama, M. Ohshita, A. Nijubu, H. Nishikawa, H. Yanase, J. Hayashi, et al., Carbon 44 (9) (2006) 1754–1761, http://dx.doi.org/10.1016/j.carbon.2005.12.039.
[7] Q. Zhang, J. Liu, R. Sager, L. Dai, J. Baur, Compos. Sci. Technol. 69 (5) (2009) 594–601, http://dx.doi.org/10.1016/j.compscitech.2008.12.002.
[8] R. Cartwright, S. Esconjauregui, D. Hardeman, S. Bhardwaj, R. Weatherup, Y. Guo, et al., Carbon 81 (2015) 639–649, http://dx.doi.org/10.1016/j.carbon.2014.10.001.
[9] N. De Greef, L. Zhang, A. Magrez, L. Forró, J.-P. Locquet, I. Verpoest, et al., Diam. Relat. Mater. 51 (2015) 39–48, http://dx.doi.org/10.1016/j.diamond.2014.11.002.
[10] R. Li, N. Lachman, P. Florin, H.D. Wagner, B.L. Wardle, Compos. Sci. Technol. 117 (2015) 139–145, http://dx.doi.org/10.1016/j.compscitech.2015.04.014.
[11] S.A. Steiner, R. Li, B.L. Wardle, ACS Appl. Mater. Interfaces 5 (11) (2013) 4892–4903, http://dx.doi.org/10.1021/am4006385.
[12] S. Vogel, C. Dransfeld, B. Friedler, J. Gobrecht, in: Proceeding of the 16th European Conference on Composite Materials Seville, Spain, June 22-26, 2014. ISBN 978-84-616-9798-4.
[13] R. Warren, C.H. Anderson, M. Carlsson, J. Mater. Sci. 13 (1) (1978) 178–188, http://dx.doi.org/10.1007/BF00739289.
[14] W. Szmyt, S. Vogel, M. Holler, A. Diaz, J. Gobrecht, M. Calame, et al., in: Proceeding of the 17th European Conference on Composite Materials, Munich, Germany, June 26-30, 2016. ISBN 978-3-00-053387-7.
[15] M. Dierolf, A. Menzel, P. Thibault, P. Schneider, C.M. Kewish, R. Wepf, et al., Nature 467 (7314) (2010) 436–439, http://dx.doi.org/10.1038/nature09419.
[16] A. Diaz, M. Guizar-Sicairos, A. Poeppel, A. Menzel, O. Bunk, Carbon 67 (2014) 98–103, http://dx.doi.org/10.1016/j.carbon.2013.09.066.
[17] M. Holler, A. Diaz, M. Guizar-Sicairos, P. Karvinen, E. Färm, E. Härkönen, et al., Sci. Rep. 4 (2014) 3857, http://dx.doi.org/10.1038/srep03857.
[18] S.M. George, Chem. Rev. 110 (1) (2010) 111–131, http://dx.doi.org/10.1021/cr900056b.
[19] J.M. Rodenburg, A.C. Hurst, A.G. Cullis, B.R. Dobson, F. Pfeiffer, O. Bunk, et al., Phys. Rev. Lett. 98 (3) (2007), http://dx.doi.org/10.1103/PhysRevLett.98.034801.
[20] H.M.L. Faulkner, J.M. Rodenburg, Phys. Rev. Lett. 93 (2) (2004), http://dx.doi.org/10.1103/PhysRevLett.93.023903.
[21] P. Thibault, M. Dierolf, A. Menzel, O. Bunk, C. David, F. Pfeiffer, Science 321 (5887) (2008) 379–382, http://dx.doi.org/10.1126/science.1158573.
[22] P. Thibault, M. Guizar-Sicairos, New J. Phys. 14 (6) (2012) 063004, http://dx.doi.org/10.1088/1367-2630/14/6/063004.
[23] M. Guizar-Sicairos, A. Diaz, M. Holler, M.S. Lucas, A. Menzel, R.A. Wepf, et al., Opt. Express 19 (22) (2011) 21345, http://dx.doi.org/10.1364/OE.19.021345.
[24] M. Guizar-Sicairos, J.J. Boon, K. Mader, A. Diaz, A. Menzel, O. Bunk, Optica 2 (3) (2015) 259, http://dx.doi.org/10.1364/OPTICA.2.000259.
[25] M. van Heel, M. Schatz, J. Struct. Biol. 151 (3) (2005) 250–262, http://dx.doi.org/10.1016/j.jsb.2005.05.009.
[26] M. Perezcabero, J. Catal. 215 (2) (2003) 305–316, http://dx.doi.org/10.1016/S0021-9517(03)00026-5.
[27] A.K. Schaper, H. Hou, A. Greiner, F. Phillipp, J. Catal. 222 (1) (2004) 250–254, http://dx.doi.org/10.1016/j.jcat.2003.11.011.
[28] M.D. Groner, F.H. Fabreguette, J.W. Elam, S.M. George, Chem. Mater. 16 (4) (2004) 639–645, http://dx.doi.org/10.1021/cm0304546.
[29] F.W. von Batchelder, R.F. Raeuchle, Acta Crystallogr. 7 (5) (1954) 464, http://dx.doi.org/10.1107/S0365110X54001466.
[30] I.G. Wood, L. Vočadlo, K.S. Knight, D.P. Dobson, W.G. Marshall, G.D. Price, et al., J. Appl. Crystallogr. 37 (1) (2004) 82–90, http://dx.doi.org/10.1107/S0021889803024695.
[31] J.C. Lagarias, J.A. Reeds, M.H. Wright, P.E. Wright, SIAM J. Optim. 9 (1) (1998) 112–147, http://dx.doi.org/10.1137/S1052623496303470.
[32] M. Kumar, Y. Ando, J. Nanosci. Nanotechnol. 10 (6) (2010) 3739–3758, http://dx.doi.org/10.1166/jnn.2010.2939.
[33] A.W. Bowman, A. Azzalini, Applied smoothing techniques for data analysis: the kernel approach with S-plus illustrations. Oxford Statistical Science Series vol. 18, OUP Oxford, 1997, pp. 6–10 (Chapter 1.3).
[34] S. Gorelick, V.A. Guzenko, J. Vila-Comamala, C. David, Nanotechnology 21 (29) (2010) 295303, http://dx.doi.org/10.1088/0957-4484/21/29/295303.

[35] X. Huang, H. Yan, R. Harder, Y. Hwu, I.K. Robinson, Y.S. Chu, Opt. Express 22 (10) (2014) 12634, http://dx.doi.org/10.1364/OE.22.012634.
[36] R. Dinapoli, A. Bergamaschi, B. Henrich, R. Horisberger, I. Johnson, A. Mozzanica, et al., Nucl. Instrum. Methods Phys. Res. Sect. Accel. Spectrom. Detect. Assoc. Equip. 650 (1) (2011) 79–83, http://dx.doi.org/10.1016/j.nima.2010.12.005.
[37] M. Dierolf, Ptychographic X-ray Microscopy and Tomography (Chapter 7), Technical University Munich Germany, 2015. PhD thesis.